chemical source in the proposed Gerst and Quay isotopic budget, we note that our budget assumes thermodynamic equilibrium between H_2 and H_2O for the highly depleted oceanic and N_2 fixation sources ($\delta D_{H2} \approx -700‰$), whereas Gerst and Quay included these terms with photochemical production. If these minor sources are indeed extremely depleted, as observed for other biogenic sources[6], they will have considerable effect on the isotopic budget. Future research will need to address details such as these to improve upon the isotopic budget estimates. □

Methods

Isotopic notation

$\delta D = (R_{sample}/R_{reference} - 1) \times 1,000$, where R_i is the D/H ratio and the reference is Vienna Standard Mean Ocean Water.

Sampling

Samples were collected from the NASA ER-2 aircraft[13] in January–March 2000 between 65–80 °N, 13–63 °E and 11–21 km altitude during the Sage III Ozone Loss and Validation Experiment[26]. Duplicate analyses of selected samples that were transferred to glass flasks soon after collection showed, with only two exceptions, that H_2 and $(D/H)_{H2}$ were not affected by long-term storage in the electropolished canisters (Supplementary Information).

Box model derivation

Because $[H_2]$ is essentially constant (Fig. 2) in the stratosphere, the production rate of H_2 (P_{H2}) is approximately equal to its loss rate[15], L_{H2}, which can be expressed as:

$$\frac{d[H_2]}{dt} = P_{H2} - L_{H2} \approx 0 \quad (2)$$

Note that P_{H2} depends on the loss rate of CH_4 (L_{CH4}) because H_2 is a by-product of the photooxidation of methane (R4–R7b; Fig. 3). As only a fraction of methane loss ultimately yields H_2, we define this dependence as $P_{H2} = \gamma L_{CH4}$ where γ is the fractional yield of H_2 from CH_4. The production of HD is similarly defined as $P_{HD} = \gamma' L_{CH3D}$. The fraction of CH_3D that produces HD, γ', is not equal to γ owing to the branching and subsequent fractionations that CH_3D and its products undergo during production of HD (see Fig. 1). These terms are unknown, and defined here as the composite term α_β. We define γ' as the product of γ with this composite fractionation so that it can be rewritten as $\alpha_\beta = \gamma'/\gamma$. Then, given that $[H_2] \approx [HH]$ and that the loss rates of HD and CH_3D can be expressed as $L_{HD} = L_{HH}\alpha_{H2+ox}[HD]/[HH]$ and $L_{CH3D} = L_{CH4}\alpha_{CH4+ox}[CH_3D]/[CH_4]$, respectively, and recalling that $P_{HH} = \gamma L_{CH4}$, we derive an expression for the rate of change of HD:

$$\frac{d[HD]}{dt} = \gamma L_{CH4}\frac{[CH_3D]}{[CH_4]}\alpha_\beta\alpha_{CH4+ox} - L_{HH}\frac{[HD]}{[HH]}\alpha_{H2+ox} \quad (3)$$

Because we express our data in terms of the (D/H) ratio rather than abundances of isotopologues, we note that $(D/H)_{H2} \approx 0.5[HD]/[HH]$ and $(D/H)_{CH4} \approx 0.25[CH_3D]/[CH_4]$ and define the total fractionation in production of H_2 from CH_4 as $\overline{\alpha}_{CH4\rightarrow H2} = 2\alpha_\beta\alpha_{CH4+ox} = 2(\gamma'/\gamma)\alpha_{CH4+ox}$. It is this fractionation that determines the D content of H_2 produced from methane oxidation, and can be estimated from our stratospheric measurements of δD of H_2 and CH_4. Included in $\overline{\alpha}_{CH4\rightarrow H2}$ is the initial oxidation of CH_4, α_{CH4+ox}, as well as all subsequent branching and fractionation, α_β, in the formation of H_2. Using the relationships above, and recalling that we assume [HH] to be constant, equation (3) can be rewritten as:

$$\frac{d(D/H)_{H2}}{dt} = [HH]^{-1}[\gamma L_{CH4}(D/H)_{CH4}\overline{\alpha}_{CH4\rightarrow H2} - L_{HH}(D/H)_{H2}\alpha_{H2+ox}] \quad (4)$$

We then combine equation (4) with the measurements of $(D/H)_{H2}$ reported here and of $(D/H)_{CH4}$ for the same suite of samples[12] along with the assumptions described in the text in order to solve for $\overline{\alpha}_{CH4\rightarrow H2}$.

Received 24 January; accepted 15 July 2003; doi:10.1038/nature01917.

1. Novelli, P. C. *et al.* Molecular hydrogen in the troposphere: Global distribution and budget. *J. Geophys. Res.* **104,** 30427–30444 (1999).
2. Ehhalt, D., Israel, G., Roether, W. & Stich, W. Tritium and deuterium content of atmospheric hydrogen. *J. Geophys. Res.* **68,** 3747–3751 (1963).
3. Gonsior, B., Friedman, I. & Lindenmayr, G. New tritium and deuterium measurements in atmospheric hydrogen. *Tellus* **XVIII,** 256–261 (1966).
4. Friedman, I. & Scholz, T. G. Isotopic composition of atmospheric hydrogen, 1967–1969. *J. Geophys. Res.* **79,** 785–788 (1974).
5. Gerst, S. & Quay, P. Deuterium component of the global molecular hydrogen cycle. *J. Geophys. Res.* **106,** 5021–5031 (2001).
6. Rahn, T., Kitchen, N. & Eiler, J. M. D/H ratios of atmospheric H_2 in urban air: Results using new methods for analysis of nano-molar H_2 samples. *Geochim. Cosmochim. Acta* **66,** 2475–2481 (2002).
7. Blake, D. R. & Rowland, F. S. Urban leakage of liquified petroleum gas and its impact on Mexico City air quality. *Science* **269,** 953–956 (1995).
8. Chen, T. Y., Simpson, I. J., Blake, D. R. & Rowland, F. S. Impact of the leakage of liquefied petroleum gas (LPG) on Santiago air quality. *Geophys. Res. Lett.* **28,** 2193–2196 (2001).
9. Gerst, S. & Quay, P. The deuterium content of atmospheric molecular hydrogen: Method and initial measurements. *J. Geophys. Res.* **105,** 26433–26445 (2000).
10. Ehhalt, D. H., Davidson, J. A., Cantrell, C. A., Friedman, I. & Tyler, S. The kinetic isotope effect in the reaction of H_2 with OH. *J. Geophys. Res.* **94,** 9831–9836 (1989).
11. Khalil, M. A. K. & Rasmussen, R. A. Global increase of atmospheric molecular hydrogen. *Nature* **347,** 743–745 (1990).
12. Rice, A. L., Tyler, S., McCarthy, M. C., Boering, K. A. & Atlas, E. The carbon and hydrogen isotopic composition of stratospheric methane: Part 1. High-precision observations from the NASA ER-2 aircraft. *J. Geophys. Res.* doi:10.1029/2002JD003042 (in the press).
13. Schauffler, S. M. *et al.* Chlorine budget and partitioning during the Stratospheric Aerosol and Gas Experiment (SAGE) III Ozone Loss and Validation Experiment (SOLVE). *J. Geophys. Res.* **108,** doi:101029/2001JGD002040 (2003).
14. Boering, K. A. *et al.* Stratospheric mean ages and transport rates from observations of carbon dioxide and nitrous oxide. *Science* **274,** 1340–1343 (1996).
15. Hurst, D. F. *et al.* Closure of the total hydrogen budget of the northern extratropical lower stratosphere. *J. Geophys. Res.* **104,** 8191–8200 (1999).
16. Robert, F. & Epstein, S. The concentration and isotopic composition of hydrogen, carbon, and nitrogen in carbonaceous meteorites. *Geochim. Cosmochim. Acta* **46,** 81–95 (1982).
17. Leshin, L. A., Epstein, S. & Stolper, E. M. Hydrogen isotope geochemistry of SNC meteorites. *Geochim. Cosmochim. Acta* **60,** 2635–2650 (1996).
18. Moortgat, G., Seiler, W. & Warneck, P. Photodissociation of HCHO in air—CO and H_2 quantum yields at 220 and 300 K. *J. Chem. Phys.* **78,** 1185–1190 (1983).
19. Brasseur, G. & Solomon, S. *Aeronomy of the Middle Atmosphere* (Reidel, Dordrecht, 1984).
20. DeMore, W. B. *et al. Chemical Kinetics and Photochemical Data for Use in Stratospheric Modeling* 278 (NASA-JPL, Pasadena, 1997).
21. Talukdar, R. K. *et al.* Kinetics of hydroxyl radical reactions with isotopically labeled hydrogen. *J. Phys. Chem.* **100,** 3037–3043 (1996).
22. Talukdar, R. K. & Ravishankara, A. R. Rate coefficients for $O(^1D) + H_2$, D_2, HD reactions and H atom yield in $O(^1D)$ + HD reaction. *Chem. Phys. Lett.* **253,** 177–183 (1996).
23. Taatjes, C. A. Infrared frequency-modulation measurements of absolute rate coefficients for Cl + HD → HCl(DCl) + D(H) between 295 and 700 K. *Chem. Phys. Lett.* **306,** 33–40 (1999).
24. Hauglustaine, D. A. & Ehhalt, D. H. A three-dimensional model of molecular hydrogen in the troposphere. *J. Geophys. Res.* **107,** doi:10.1029/2001JD001156 (2002).
25. Holton, J. R. On the global exchange of mass between the stratosphere and troposphere. *J. Atmos. Sci.* **47,** 392–395 (1990).
26. Newman, P. A. *et al.* An overview of the SOLVE/THESEO 2000 campaign. *J. Geophys. Res.* **107,** doi:101029/2001JD001303 (2002).
27. Saueressig, G. *et al.* Carbon 13 and D kinetic isotope effects in the reactions of CH_4 with $O(^1D)$ and OH: New laboratory measurements and their implications for the isotopic composition of stratospheric methane. *J. Geophys. Res.* **106,** 23127–23138 (2001).
28. Saueressig, G., Bergamaschi, P., Crowley, J. N., Fischer, H. & Harris, G. W. D/H kinetic isotope effect in the reaction CH_4 + Cl. *Geophys. Res. Lett.* **23,** 3619–3622 (1996).

Supplementary Information accompanies the paper on **www.nature.com/nature**.

Acknowledgements We thank N. Kitchen for assistance in the laboratory. This study was supported in part by the NSF (T.A.R., K.A.B. and S.T.), the Davidow Fund and General Motors Corp. (J.M.E), the David and Lucile Packard Foundation (K.A.B.) and the NASA Upper Atmosphere Research Program (P.O.W., K.A.B, E.A, S.S. and S.D.). The National Centre for Atmospheric Research is operated by the University Corporation for Atmospheric Research under the sponsorship of the NSF. T.R. is the recipient of a Frederick Reines postdoctoral fellowship in experimental sciences awarded by Los Alamos National Laboratory.

Competing interests statement The authors declare that they have no competing financial interests.

Correspondence and requests for materials should be addressed to T.R. (trahn@lanl.gov).

Remote triggering of deep earthquakes in the 2002 Tonga sequences

Rigobert Tibi[1], Douglas A. Wiens[1] & Hiroshi Inoue[2]

[1]*Department of Earth and Planetary Sciences, Washington University, St. Louis, Missouri 63130, USA*
[2]*National Research Institute for Earth Science and Disaster Prevention, Tsukuba, Ibaraki 305-0006, Japan*

It is well established that an earthquake in the Earth's crust can trigger subsequent earthquakes, but such triggering has not been documented for deeper earthquakes. Models for shallow fault interactions suggest that static (permanent) stress changes can trigger nearby earthquakes, within a few fault lengths from the causative earthquake[1–3], whereas dynamic (transient) stresses carried by seismic waves may trigger earthquakes both nearby

and at remote distances[4–8]. Here we present a detailed analysis of the 19 August 2002 Tonga deep earthquake sequences and show evidence for both static and dynamic triggering. Seven minutes after a magnitude 7.6 earthquake occurred at a depth of 598 km, a magnitude 7.7 earthquake (664 km depth) occurred 300 km away, in a previously aseismic region. We found that nearby aftershocks of the first mainshock are preferentially located in regions where static stresses are predicted to have been enhanced by the mainshock. But the second mainshock and other triggered events are located at larger distances where static stress increases should be negligible, thus suggesting dynamic triggering. The origin times of the triggered events do not correspond to arrival times of the main seismic waves from the mainshocks and the dynamically triggered earthquakes frequently occur in aseismic regions below or adjacent to the seismic zone. We propose that these events are triggered by transient effects in regions near criticality, but where earthquakes have difficulty nucleating without external influences.

Although earthquake triggering is a well-studied phenomenon for shallow events, there has been little work on triggered deep earthquakes. Understanding the conditions under which deep earthquakes may be triggered may provide important clues about the mechanism of deep earthquakes, which is still uncertain[9–13].

On 19 August 2002, a deep earthquake of moment magnitude M_w 7.6 in the Tonga subduction zone was followed 130 seconds later by an event of body-wave magnitude M_b 5.9 located 290 km away, and an additional 311 seconds later by an M_w 7.7 earthquake near that location (Fig. 1, Table 1). For the region within about 100 km from the later earthquakes, no well-located events are found in systematic relocations (Fig. 2), suggesting that these earthquakes occurred in a previously aseismic region. Therefore, they do not represent a fortuitous occurrence of background seismicity, and their proximity in time clearly indicates a causal link between the initial event and the later earthquakes. Thus the second main event and its foreshock must have been triggered by processes following the first earthquake. The second main event, located at a depth of 664 ± 4 km is also the deepest-known event with $M_w > 7$.

Rupture details for the two main events, and aftershock locations need to be clarified to understand the triggering scenario. We combined teleseismic arrival times with regional data to constrain the location of both sequences (see Methods). One foreshock and 21 aftershocks are reported for the first sequence. The second sequence consists of the foreshock mentioned above and three aftershocks (see Supplementary Table 2). Results of body waveform inversion (see Methods) suggest that the first main event consists of three episodes of moment release (Supplementary Table 3 and Supplementary Fig. 5). Rupture propagated mainly northward, consistent with the location of most aftershocks (Fig. 1a). However, some events are also located south of the main-event initiation point. Results of stress-transfer calculations (discussed later) suggest that events located south from the mainshock initiation point are related to a southward expansion of the aftershock activity, resulting from Coulomb stress increase in that area (Fig. 3). The overall mechanism for the mainshock consists of a north–south striking and steeply dipping nodal plane, and a northwest–southeast trending subhorizontal nodal plane. Given the east–west rupture extent of only ~30 km (Fig. 1), the vertical component of rupture of about 40 km cannot be accommodated along the subhorizontal

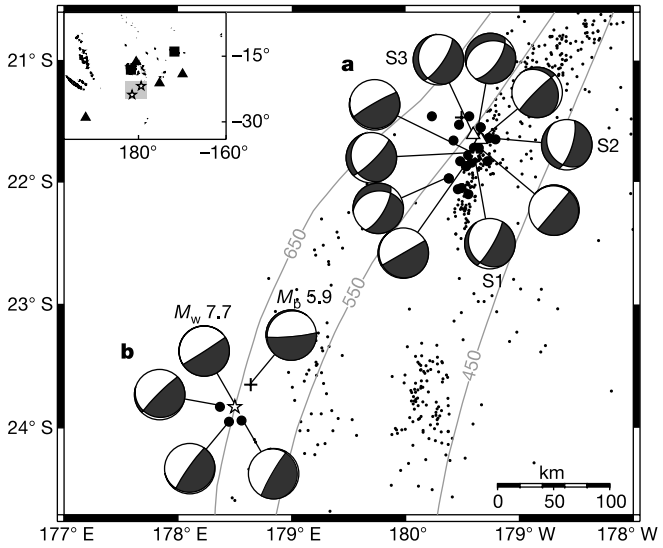

Figure 1 Epicentral locations of the two 2002 Tonga deep earthquake sequences. Dots, the locations of previous earthquakes[33]. Grey lines, contours of deep seismicity[34] with the numbers indicating the depth in km to the seismogenic zone. Fault plane solutions are lower-hemisphere projections of the focal spheres. Black and white quadrants indicate compressional and tensional areas, respectively. **a** Star, the epicentre (S1) of the initial earthquake (M_w 7.6, depth 598 km), triangles, its second (S2) and third (S3) episodes of rupture, as inferred from the body-wave inversion (see Methods and Supplementary Table 3). Cross, a foreshock that occurred 8 days before the main event. Circles, aftershocks (Supplementary Table 2). The distribution of aftershocks excluding events located south of the mainshock epicentre (discussed in text) indicates an east–west and vertical rupture extent of about 30 km and 40 km, respectively. **b** Locations of the triggered earthquake (star) (M_w 7.7, depth 664 km), and its aftershocks (circles). Cross, a foreshock that occurred about five minutes before the main event. Inset, the locations of the SPANET (triangles) and the regional stations AFI and MSVF of the Global Seismic Network (squares) used in combination with teleseismic stations to locate both earthquake sequences. The SPANET network consists of broadband seismic stations operated in several islands in the Southwest Pacific. Stars in the inset, the epicentres of the 2002 mainshocks.

Table 1 **Triggered deep earthquakes**

Initial event		Triggered Event		Mag.	Depth (km)	ΔT (min:s)	Dist. (km)	v_{st} (km s^{-1})	Notes
Date	OT (h:min:s)	Date	OT (h:min:s)						
19 Aug 2002	11:01:04			7.6	598				Tonga region
		19 Aug 2002	11:03:14	5.9	647	2:10	290	2.23	Nearly aseismic area
		19 Aug 2002	11:08:25	7.7	664	7:21	313	0.71	
09 Mar 1994	23:28:08			7.6	563				Tonga region
		10 Mar 1994	00:43:08	5.2	609	75:00	105	0.02	In slab
		10 Mar 1994	01:51:41	5.0	637	143:33	72	0.01	Nearly aseismic area
09 Jun 1994	00:33:17			8.3	640				Bolivia region
		09 Jun 1994	01:15:18	5.9	650	42:01	84	0.03	Aseismic region
26 May 1986	18:40:45			6.8	590				Tonga region
		26 May 1986	19:06:16	7.1	543	25:31	257	0.17	Nearly aseismic area
		26 May 1986	19:48:37	5.4	633	67:52	317	0.08	
21 Jul 1994	18:36:33			7.3	473				Japan Sea
		21 Jul 1994	18:55:59	5.9	514	19:26	127	0.11	In slab

OT, event origin time. ΔT, the separation in origin time. Dist., the epicentral distance between the causative earthquake and the triggered event. v_{st}, the estimated apparent stress pulse velocity.

nodal plane. An inversion for the plane that best fits the aftershock locations, excluding the triggered events (discussed later), yields values of 14° for the strike and 73° for the dip, consistent with the orientation of the near-vertical nodal plane. These represent strong evidence that rupture during the first 2002 main event occurred along the near vertical plane.

For the second mainshock, both visual inspection and inversion of the waveforms show no evidence of rupture directivity. The spatial distribution of the foreshock and aftershocks do not define a consistent direction relative to the mainshock. Thus the rupture may have spread out radially, starting from the initiation point (Fig. 1b), which would explain the absence of a directivity effect. The mainshock focal mechanism shows a northeastward trending vertical nodal plane and a southwestward striking horizontal nodal plane. The three aftershocks and the main event are located approximately at the same depth of ~665 km (Fig. 2). The lateral extent, as defined by the foreshock and aftershocks, is inconsistent with the orientation of the vertical nodal plane, suggesting that the horizontal plane of the focal mechanism is probably the one that ruptured.

The Coulomb failure criterion is broadly used to describe the conditions under which shear failure occurs in rocks[14]. For shallow events, Coulomb stress increases associated with prior earthquakes have successfully explained subsequent rupture (that is triggering) on nearby and remote faults, and increases in seismicity rates[1–7]. We investigated fault interactions in the 2002 Tonga deep earthquakes (see Methods section). First, we examined the relationship between the first main event and its aftershocks. The results show that aftershocks south of the mainshock initiation point are located within and around an area where the Coulomb stress increased by about 0.2–3 MPa during the main rupture (Fig. 3). This suggests that the southern aftershocks were promoted by stress transfer from the mainshock, which may itself have been induced by the foreshock that occurred eight days earlier at a distance of about 36 km. Eight of the 11 aftershocks located more than 20 km from the main event centroid are consistent with regions of Coulomb stress increase. Similarly, the reported zone of aftershock expansion for the 1994 Tonga deep sequence[15] corresponds to a region where stress was enhanced by the main rupture.

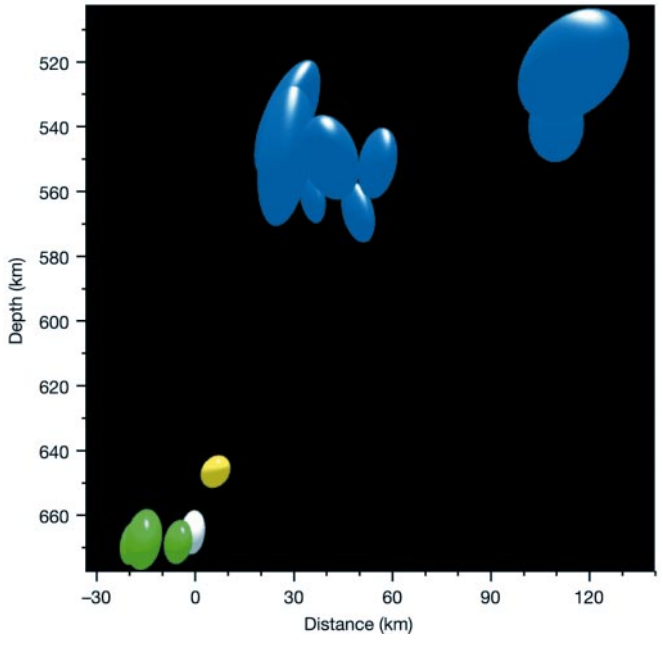

Figure 2 Vertical cross-section perpendicular to the deep Tonga slab showing the 95% confidence ellipsoid for the location of the triggered 2002 Tonga sequence. White, the main event; yellow, its foreshock; green, the aftershocks; blue, the relocated background seismicity from the latitude range between −23.25° and −24.25°, as reported in the International Seismological Centre (ISC) (1964–1989) and PDE (post-1989) catalogues. Note the lack of seismicity below about 570 km, indicating that the 2002 sequence occurred in a previously aseismic portion of the slab. Distance is measured along the northwest–southeast (N80°W to S80°E).

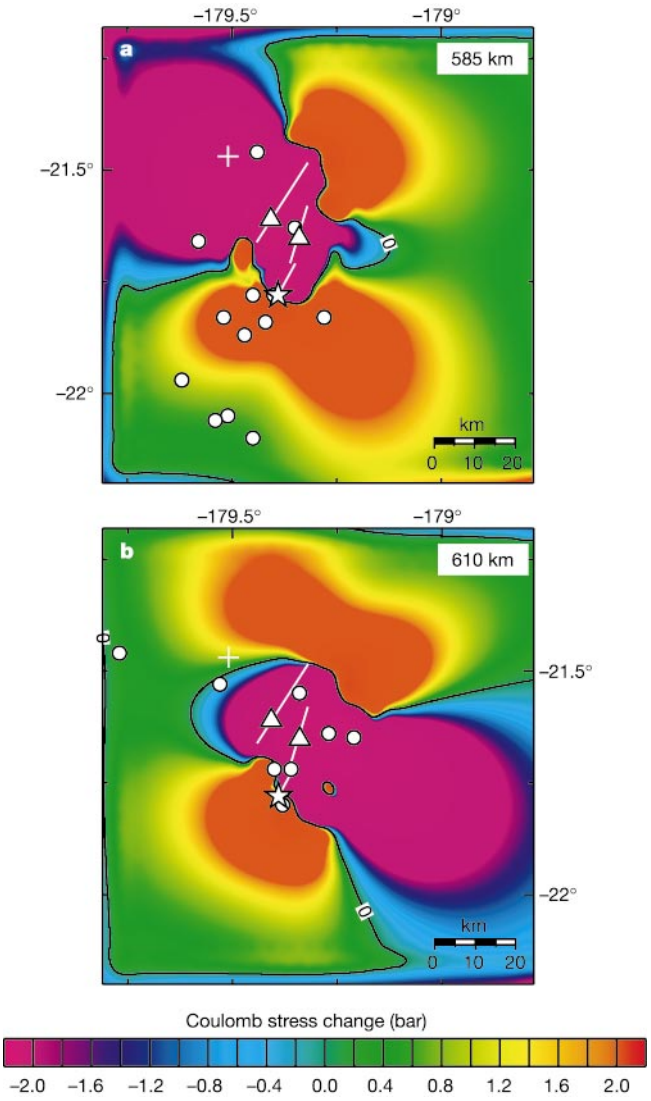

Figure 3 Map showing the location of the first sequence in the 2002 Tonga deep earthquakes, and the calculated static Coulomb stress changes at 585 km (**a**) and 610 km depth (**b**) associated with the mainshock (see Methods). For the short timescale corresponding to the aftershock sequence, the deformation in the relatively rigid subducting plate can be approximated by elastic responses to the fault slip. We applied an approach commonly used for shallow events[1,32] to compute the co-seismic static stress changes. Because the near–vertical plane ruptured during the first mainshock, the Coulomb stress changes shown have been resolved on a fault whose orientation and slip direction correspond to the average strike, dip and rake of the near-vertical nodal plane of the aftershock focal mechanisms (Fig. 1a). Black lines, zero contours. Star, the relocated mainshock epicentre; triangles, its second and third subevents, as inferred from the body-wave inversion (Supplementary Table 3). Cross, the foreshock; and circles, the aftershocks. Aftershocks plotted in **a** and **b** are those with focal depth ≤600 km and >600 km, respectively. White lines represent the three subfaults in accordance with the best-fitting rupture model of the main event. The fault lengths have been estimated from subevent duration (see Supplementary Fig. 5b) for the best-fitting rupture velocity of 3 km s^{-1}. Note aftershocks south of the mainshock initiation point in **a**. These events are located within and around an area where the Coulomb stress increased by about 2–30 bar.

Calculations of static Coulomb stress changes induced by the first main event on the second mainshock fault show extremely small changes, because the second 2002 Tonga sequence occurred about 300 km (approximately ten source dimensions) away. This can be anticipated from the rapid decay with distance (approximately as $1/r^3$ to $1/r^2$) for static stress changes[16], and indicates that these could not be the triggering agents for the second sequence.

Dynamic strains carried by seismic waves can reduce the frictional strength of faults, promoting their failure and inducing earthquakes[17]. Because dynamic strains may occur far from the source, dynamic triggering has been put forward to explain failure at remote distance from an initial earthquake[4,8]. The northward rupture propagation for the first main event in the 2002 Tonga deep earthquakes is expected to focus seismic waves toward the north, resulting in larger dynamic strains that may favour earthquake triggering in that direction[16,18]. The location of the triggered sequence rather southwest of the initial earthquake, in an aseismic area, indicates that pre-existing conditions, such as prevailing high stresses, may have been particularly favourable to rupture in that region. The fault must have been in a critical state (close to failure) prior to the arrival of inducing strain pulses.

We have surveyed catalogues of deep earthquakes and include prominent examples of aftershocks triggered at substantial distances in Table 1. Deep earthquakes are commonly triggered in the initial three hours at distances of 50–300 km, well outside the faulting and aftershock zone of the causative event. Static Coulomb stress changes at these distances are small, suggesting that most of these events are dynamically triggered. In most cases, the triggered earthquakes occur in largely aseismic regions, either below or displaced laterally from the active seismic zone. A prominent example is the 26 May 1986 Tonga sequence, in which a M_w 7.1 event occurred in an aseismic region 25 minutes after a M_w 6.8 slab earthquake at a distance of 257 km (Fig. 4). A smaller earthquake occurred further west an additional 42 minutes later. The triggered (outboard) earthquakes are located in a remnant slab that lies subhorizontally above the active, steeply dipping Tonga deep zone[19,20]. Aftershock activity continued in the outboard region for 14 days, after which an M_w 7.0 earthquake occurred near the initial event. Assuming a typical rupture length for deep earthquakes with this magnitude[21] implies that the triggering process operated at a distance of 15–20 fault lengths. The longer duration for the triggered activity suggests that transient processes were not the sole mode of triggering involved. Static loads induced by the triggered M_w 7.1 event may have promoted the later aftershocks in its vicinity.

The occurrence of triggered events in aseismic portions of the slab suggests that these areas may be near criticality. Rupture initiation may be difficult in these regions[12,22], such that events are readily triggered by processes following earthquakes in adjacent seismically active zones. These regions can also sustain seismic rupture if an event initiated in the seismically active zone propagates into the surrounding material[22]. The spatio-temporal separations between the triggering and triggered earthquakes do not define a consistent stress pulse velocity. Instead, the effective propagation velocity of the triggering mechanism varies greatly from a few metres per second up to more than 2 km s^{-1} (Table 1). Because deep earthquakes do not generate surface waves, only body waves are likely to be carriers of dynamic strains. The triggered earthquakes occurred tens of seconds to a few hours after the passage of P and S waves from the causative event, indicating that a short-term delay mechanism may be involved, as observed for shallow earthquakes[4,6].

Phenomena such as fluid diffusion, viscoelastic relaxation and fault frictional properties are believed to control delayed triggering for shallow earthquakes[6,8,23–25]. The first two mechanisms involve longer characteristic times that are inconsistent with the time delays (tens of seconds to a few hours) observed in this study. For shallow faults, rate- and state-dependent friction laws could possibly explain short time delays[26]. Although frictional laws may not apply directly to deep earthquake failure, other mechanisms with short delay times may be operating. For example, the development of adiabatic

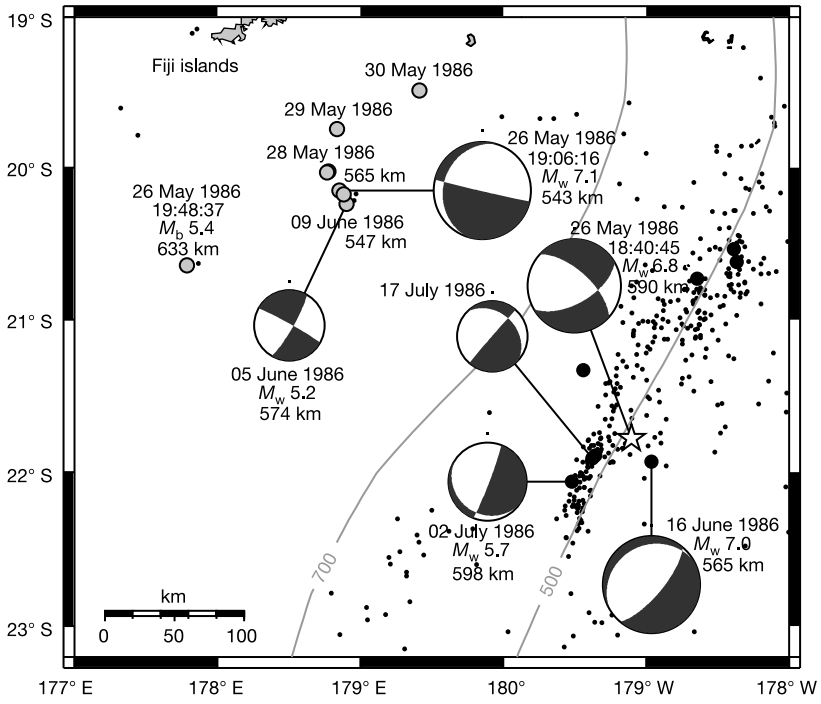

Figure 4 The 1986 Tonga sequence. Star, the initial event. Slab earthquakes are denoted by black circles. Triggered outboard events are represented by grey circles. Focal mechanisms are from the Harvard Centroid Moment Tensor (CMT) catalogue[35], with the projection size proportional to the seismic moment. Black and white areas are compressional and tensional, respectively. The origin time, the magnitude and the depth of the earthquakes are indicated. Dots, the background seismicity[33]. Grey lines, contours of deep seismicity[34] with the numbers indicating the depth in km to the seismogenic zone.

plastic instabilities[27–29] may incorporate a time dependence that may serve as a nonlinear temperature-dependent delay factor in dynamic triggering. We purpose that deep events can be remotely triggered by transient effects incorporating such nonlinear short-term delay mechanisms in regions where high stress may predominate, but where earthquakes have difficulty nucleating without external influences. □

Methods

Aftershock location

We combined teleseismic arrival times from the Preliminary Determination of Epicentres (PDE) with regional data from the SPANET network (Fig. 1) to constrain the location of the 2002 sequences. P, pP, sP and regional S arrival times were inverted using a hypocentroidal decomposition method that minimizes the effect of velocity heterogeneities along the ray paths[30]. Two stations of the Global Seismic Network (GSN), AFI and MSVF, and stations of the SPANET network, located at distances of about 5–13° (Fig. 1), recorded upgoing P and/or S phases that allowed better depth constraints.

Body-waveform inversion

Using global broadband data, we inverted for the source parameters of both mainshocks[21,31]. Global data were combined with recordings of the SPANET network to infer the focal mechanism of the larger (M_b >4.6) aftershocks with a grid search method that fits P and SH waveforms simultaneously.

Coulomb failure stress

The Coulomb failure stress change is expressed as $\Delta\sigma_f = \Delta\tau + \mu'\Delta\sigma$, where $\Delta\tau$ is the shear stress change on a fault (positive in the direction of fault slip), $\Delta\sigma$ is the normal stress change (positive for extension), and μ' is the apparent coefficient of friction, which includes the effects of pore pressure change. Failure is promoted if $\Delta\sigma_f$ is positive and inhibited if negative [1,32]. The Coulomb stress changes are computed in an elastic half-space using the finite-fault source model for the initial event which consists of three subfaults (Supplementary Table 3). For each subfault, an uniform slip distribution, consistent with the estimated average dislocation of 2 m, is used. Aftershocks located in the depth range between 579 km ad 623 km imply widths of about 40 km for the near vertical subfaults. In the calculations, we assumed a shear modulus of 11.6×10^{11} dyn cm^{-2}, appropriate for a depth of 571 km, and a Poisson's ratio of 0.24 for olivine, the dominant mineral in mantle. For the apparent coefficient of friction μ', we employed values ranging from 0.6 to 0.9. The general stress distribution was similar for all these values. The final models were computed for $\mu' = 0.7$.

Received 18 April; accepted 14 July 2003; doi:10.1038/nature01903.

1. King, G. C. P., Stein, R. S. & Lin, J. Static stress changes and the triggering of earthquakes. *Bull. Seismol. Soc. Am.* **84,** 935–953 (1994).
2. Harris, R. A. Introduction to special section: stress triggers, stress shadows, and implications for seismic hazard. *J. Geophys. Res.* **103,** 24347–24358 (1998).
3. Stein, R. S. The role of stress transfer in earthquake occurrence. *Nature* **402,** 605–609 (1999).
4. Hill, D. P. *et al.* Seismicity remotely triggered by the magnitude 7.3 Landers, California, earthquake. *Science* **260,** 1617–1623 (1993).
5. Harris, R. A. & Day, S. M. Dynamics of faults interaction: parallel strike-slip faults. *J. Geophys. Res.* **98,** 4461–4472 (1993).
6. Belardinelli, M. E., Cocco, M., Coutant, O. & Cotton, F. Redistribution of dynamic stress during coseismic ruptures: evidence for fault interaction and earthquake triggering. *J. Geophys. Res.* **104,** 14925–14945 (1999).
7. Kilb, D., Gomberg, J. & Bodin, P. Triggering of earthquake aftershocks by dynamic stresses. *Nature* **408,** 570–574 (2000).
8. Gomberg, J., Blanpied, M. L. & Beeler, N. M. Transient triggering of near and distant earthquakes. *Bull. Seismol. Soc. Am.* **87,** 295–309 (1997).
9. Frohlich, C. The nature of deep-focus earthquakes. *Annu. Rev. Earth Planet. Sci.* **17,** 227–254 (1989).
10. Green, H. W. & Houston, H. The mechanics of deep earthquakes. *Annu. Rev. Earth Planet. Sci.* **23,** 169–213 (1995).
11. Kirby, S. H., Stein, S., Okal, E. A. & Rubie, D. C. Metastable mantle phase transformations and deep earthquake in subducting oceanic lithosphere. *Rev. Geophys.* **34,** 261–306 (1996).
12. Wiens, D. A. Seismological constraints on the mechanism of deep earthquakes: temperature dependence of deep earthquake source properties. *Phys. Earth. Planet. Inter.* **127,** 145–163 (2001).
13. Tibi, R., Bock, G. & Wiens, D. A. Source characteristics of large deep earthquakes: constraint on the faulting mechanism at great depths. *J. Geophys. Res.* **108,** doi:101029/2002JB001948 (2003).
14. Jaeger, J.C. & Cook, N.G.W. *Fundamentals of Rock Mechanics* (Chapman and Hall, London, 1979).
15. Wiens, D. W. & McGuire, J. J. Aftershocks of the March 9, 1994, Tonga earthquake: the strongest known deep aftershock sequence. *J. Geophys. Res.* **105,** 19067–19083 (2000).
16. Cotton, F. & Coutant, O. Dynamic stress variations due to shear faults in a plane-layered medium. *Geophys. J. Int.* **128,** 676–688 1997).
17. Kisslinger, C. A review of theories of mechanisms of induced seismicity. *Eng. Geol.* **10,** 85–98 (1976).
18. Gomberg, J., Reasenberg, P. A., Bodin, P. & Harris, R. A. Earthquake triggering by seismic waves following the Landers and Hector Mine earthquakes. *Nature* **411,** 462–466 (2001).
19. Van der Hilst, R. D. Complex morphology of subducted lithosphere in the mantle beneath the Tonga trench. *Nature* **374,** 154–157 (1995).
20. Chen, W.-P. & Brudzinski, M. R. Evidence for a large-scale remnant of subducted lithosphere beneath Fiji. *Science* **292,** 2475–2479 (2001).
21. Tibi, R. *Untersuchungen der Ursache von Tiefherdbeben mit Hilfe von Breitbandseismogrammen. Scientific Technical Report STR00/08* (GeoForschungsZentrum Potsdam, Potsdam, 2000).
22. McGuire, J. J., Wiens, D. A., Shore, P. J. & Bevis, M. G. The March 9, 1994 (M_w 7.6), deep Tonga earthquake: rupture outside the seismically active slab. *J. Geophys. Res.* **102,** 15163–15182 (1997).
23. Hudnut, K. W., Seeber, L. & Pacheco, J. Cross-fault triggering in the November 1987 Superstition Hills earthquake sequence, Southern California. *Geophys. Res. Lett.* **16,** 199–202 (1989).
24. Freed, A. M. & Lin, J. Delayed triggering of the 1999 Hector Mine earthquake by viscoelastic stress transfer. *Nature* **411,** 180–183 (2001).
25. Pollitz, F. F. & Sacks, I. S. The 1995 Kobe, Japan, earthquake: a long-delayed aftershock of the offshore 1944 Tonankai and 1946 Nankaido earthquakes. *Bull. Seismol. Soc. Am.* **87,** 1–7 (1997).
26. King, G. C. P. & Cocco, M. Fault interaction by elastic stress changes: new clues from earthquake sequences. *Adv. Geophys.* **44,** 1–38 (2000).
27. Ogawa, M. Shear instability in a viscoelastic material as the cause of deep focus earthquakes. *J. Geophys. Res.* **92,** 13801–13810 (1987).
28. Hobbs, B. E. & Ord, A. Plastic instabilities: implications for the origin of intermediate and deep focus earthquakes. *J. Geophys. Res.* **93,** 10521–10521 (1988).
29. Karato, S., Riedel, M. R. & Yuen, D. A. Rheological structure and deformation of subducted slabs in the mantle transition zone: implications for mantle circulation and deep earthquakes. *Phys. Earth Plant. Inter.* **127,** 83–108 (2001).
30. Jordan, T. H. & Sverdrup, K. A. Teleseismic location techniques and their application to earthquake clusters in the South-Central Pacific. *Bull. Seismol. Soc. Am.* **71,** 1105–1130 (1981).
31. Nábělek, J. L., *Determination of Earthquake Source Parameters from Inversion of Body Waves.* PhD thesis, MIT (1984).
32. Toda, S., Stein, R. S., Reasenberg, P. A., Dieterich, J. H. & Yoshida, A. Stress transferred by the 1995 M_w = 6.9 Kobe, Japan, shock: effect on aftershocks and future earthquake probabilities. *J. Geophys. Res.* **103,** 24543–24565 (1998).
33. Engdahl, E. R., van der Hilst, R. & Buland, R. Global teleseismic earthquake relocation with improved travel times and procedures for depth determination. *Bull. Seismol. Soc. Am.* **88,** 722–742 (1998).
34. Gudmundsson, Ó. & Sambridge, M. A regionalized upper mantle (RUM) seismic model. *J. Geophys. Res.* **103,** 7121–7136 (1998).
35. Dziewonski, A. M., Chou, T.-A. & Woodhouse, J. H. Determination of earthquake source parameters from waveform data for studies of global and regional seismicity. *J. Geophys. Res.* **86,** 2825–2852 (1981).

Supplementary Information accompanies the paper on **www.nature.com/nature**.

Acknowledgements We thank D. Suetsugu and the operators of the SPANET network for their efforts, R. Stein for making his code available, and J. Conder and N. Kagotho for reading the manuscript. Waveforms data were supplied by the Incorporated Research Institutions for Seismology (IRIS), Geoscope, and GeoForschungsNetz (GEOFON). Arrival time data were obtained from the ISC and PDE (US Geological Survey). This research was supported by the National Science Foundation.

Competing interests statement The authors declare that they have no competing financial interests.

Correspondence and requests for materials should be addressed to R.T. (tibi@seismo.wustl.edu).

Xenoturbella is a deuterostome that eats molluscs

Sarah J. Bourlat[1], Claus Nielsen[2], Anne E. Lockyer[3], D. Timothy J. Littlewood[3] & Maximilian J. Telford[1]

[1]*University Museum of Zoology, Department of Zoology, Downing Street, Cambridge CB2 3EJ, UK*
[2]*Zoological Museum (University of Copenhagen), Universitetsparken 15, DK-2100 Copenhagen, Denmark*
[3]*Department of Zoology, The Natural History Museum, Cromwell Road, London SW7 5BD, UK*

***Xenoturbella bocki*, first described in 1949 (ref. 1), is a delicate, ciliated, marine worm with a simple body plan: it lacks a through gut, organized gonads, excretory structures and coelomic cavities. Its nervous system is a diffuse nerve net with no brain. *Xenoturbella*'s affinities have long been obscure and it was initially linked to turbellarian flatworms[1]. Subsequent authors considered it variously as related to hemichordates and echinoderms owing to similarities of nerve net and epidermal ultrastructure[2,3], to acoelomorph flatworms based on body plan and ciliary ultrastructure[4–6] (also shared by hemichordates[7]), or as among the most primitive of Bilateria[8]. In 1997 two papers seemed to solve this uncertainty: molecular phylogenetic**